Effective Viscosity, Resistivity, and Reynolds Number in Weakly Collisional Plasma Turbulence

Yan Yang,[1]* William H. Matthaeus,[1] Sean Oughton,[2] Riddhi Bandyopadhyay,[3] Francesco Pecora,[1] Tulasi N. Parashar,[4] Vadim Roytershteyn,[5] Alexandros Chasapis,[6] and Michael A. Shay[1]

[1]*Department of Physics and Astronomy, University of Delaware, Newark, DE 19716, USA*

[2]*Department of Mathematics, University of Waikato, Hamilton 3240, New Zealand*

[3]*Department of Astrophysical Sciences, Princeton University, Princeton, NJ 08544, USA*

[4]*School of Chemical and Physical Sciences, Victoria University of Wellington, Wellington 6012, New Zealand*

[5]*Space Science Institute, Boulder, CO 80301, USA*

[6]*Laboratory for Atmospheric and Space Physics, University of Colorado Boulder, Boulder, CO 80309, USA*

7 September 2023

ABSTRACT

We examine dissipation and energy conversion in weakly collisional plasma turbulence, employing *in situ* observations from the Magnetospheric Multiscale (MMS) mission and kinetic Particle-in-Cell (PIC) simulations of proton-electron plasma. A previous result indicated the presence of viscous-like and resistive-like scaling of average energy conversion rates—analogous to scalings characteristic of collisional systems. This allows for extraction of collisional-like coefficients of *effective* viscosity and resistivity, and thus also determination of effective Reynolds numbers based on these coefficients. The effective Reynolds number, as a measure of the available bandwidth for turbulence to populate various scales, links macro turbulence properties with kinetic plasma properties in a novel way.

1 INTRODUCTION

Energy dissipation in fluids and plasmas may be effectively defined as the conversion process by which macroscopic reservoirs of energy are transformed into heat. Mechanisms of energy dissipation for weakly collisional or collisionless plasma are of central importance for addressing long-standing fundamental problems in space and astrophysics. These include, for example, the acceleration of energetic particles and the heating of the solar corona and solar wind. In collisional cases, the (viscous and resistive) dissipation is expressed in a simple form in terms of viscosity, resistivity, and spatial gradients of the velocity and magnetic fields. However, space plasmas frequently reside in (nearly) collisionless regimes, where the dissipation mechanisms are not well understood. For example, in one of the most well-studied space plasmas, the solar wind (Bruno & Carbone 2013), the collision length is of the order of 1 AU and collisions are typically too weak to establish a local equilibrium (Maxwellian particle distribution) (Marsch 2006; Verniero et al. 2020). In such cases the classical collisional approach becomes generally inapplicable, as do standard closures that describe dissipation in terms of fluid-scale variables and viscosity and resistivity.

Lacking the standard collisional closures, studies of plasma turbulence have shown increasing interest in quantifying collisionless dissipation. Investigations of collisionless dissipation have often considered one or more of the following three aspects:

(i) *Dissipation mechanisms.* Collisionless dissipation has often been described in terms of specific mechanisms such as magnetic reconnection (Retinò et al. 2007), wave-particle interaction (Markovskii et al. 2006; Howes et al. 2008; Chandran et al. 2010), and turbulence-driven intermittency (Dmitruk et al. 2004; Parashar et al. 2011). Identification of such processes affords specific physical insight. If all possible mechanisms and their relative contributions

can be identified, a full understanding of the dissipation physics may be achievable.

(ii) *Turbulence cascade.* The picture of turbulence cascade describes energy transfer across scales from an energy-containing range, through an inertial range, and into a (small-scale) dissipation range. Different dissipation proxies based on the turbulence cascade process have been adopted to estimate the dissipation rate. At energy-containing scales, the global decay rate of energy is controlled by the von Kármán decay law (de Kármán & Howarth 1938; Hossain et al. 1995; Wan et al. 2012; Zank et al. 2017). At inertial range scales, the Yaglom relation (Politano & Pouquet 1998; Sorriso-Valvo et al. 2007; Hadid et al. 2017; Andrés et al. 2019; Banerjee & Andrés 2020) has been adapted to estimate the energy transfer rate. Hellinger et al. (2022) extended this approach into the kinetic range by empirically including pressure-strain interaction effects in the kinetic range.

(iii) *Energy conversion channels.* Yet another approach to understand dissipation is to trace the flow of energy and examine energy conversion between different forms. Temperature enhancement implies increase of thermal energy and to specifically track thermal energy production requires quantification of energy supplies from energy reservoirs for each species. Two widely-invoked classes of conversion are the electric work on particles for species α, $\boldsymbol{J}_\alpha \cdot \boldsymbol{E}$ (Zenitani et al. 2011) and the pressure-strain interaction for species α, $-(\boldsymbol{P}_\alpha \cdot \nabla) \cdot \boldsymbol{u}_\alpha$ (Yang et al. 2017a,b). (We employ a familiar plasma physics notation with full definitions given in Sec. 2.) These channels play different roles: the electric work measures the release of electromagnetic energy, while the pressure-strain interaction measures the increase of thermal energy.

Collisional and collisionless dissipation obviously differ from each other, but they also share similarities. For example, in both cases, conversion of energy between different forms can be quantified in terms of pressure work and electric work. In collisional cases, however, these two channels can be further approximated as viscous dissipa-

tion via velocity gradients and resistive dissipation via electric current density (i.e, magnetic field gradients), which will be discussed in detail in Sec. 2. On the other hand, investigations using *in situ* spacecraft data (Chasapis et al. 2018; Bandyopadhyay et al. 2020a) and numerical simulations (Wan et al. 2016; Yang et al. 2017a) support a novel and less obvious idea, namely that collision*less* dissipation is also in direct association with velocity strain rate and electric current density (Bandyopadhyay et al. 2023). More specifically, by quantifying collisionless dissipation by the electric work $\boldsymbol{J}_\alpha \cdot \boldsymbol{E}$ and the pressure-strain interaction $-(\boldsymbol{P}_\alpha \cdot \nabla) \cdot \boldsymbol{u}_\alpha$, these are seen to be well correlated with, respectively, squared electric current density and squared velocity strain rate. This association stands in direct analogy to the resistive and viscous dissipation in collisional plasmas. It is natural then to inquire more deeply into the behavior of collisionless dissipation and its similarities with collisional dissipation.

Initial steps in this direction have shown two findings. First, the global average of electric work conditioned on electric current density scales as J^2, i.e., the square of the current density (Wan et al. 2016; Chasapis et al. 2018). Second, that there is a similar scaling of pressure work with respect to $D^2 = D_{ij}D_{ij}$, where D_{ij} is the traceless velocity strain rate tensor (Bandyopadhyay et al. 2023). These results provide strong evidence supporting the concept of collisional-*like* dissipation in collisionless plasmas, and, moreover, allow a novel estimation of effective viscosity and resistivity, which is then further applied to define *effective Reynolds numbers*.

Since the classical closures of viscosity and resistivity are inapplicable to collisionless plasmas, one might suspect that various features of classical turbulence theory might not be applicable, in particular regarding dissipative processes and the several length scales and dimensionless numbers related to dissipation. Even the notion of Reynolds number (Re)—which in the hydrodynamic sense is the ratio of the strengths of nonlinear and viscous effects—needs to be considered with caution in the absence of viscosity and resistivity. On the other hand a point of encouragement is that wavenumber spectra in large collisionless plasmas such as the solar wind (Bruno & Carbone 2013) often exhibit a Kolmogorov-like power-law energy spectrum (Coleman 1968) that extends from a correlation scale (Matthaeus et al. 2005) to smaller kinetic scales (Leamon et al. 1998), below which the spectrum steepens. Between these scales the power-law inertial range is expected to span a larger range when the Reynolds number is greater, by analogy with hydrodynamics.

To achieve physically motivated generalizations of Re in the collisonless case, previous studies have adopted various definitions of effective Reynolds number, often related to the ratio of an outer scale to an inner scale. For example

$$\text{Re} \approx \left(\frac{\lambda_c}{\lambda_d}\right)^{4/3} \quad \text{or} \quad \text{Re} \approx \left(\frac{\lambda_c}{\lambda_T}\right)^2, \qquad (1)$$

where λ_c is the correlation length, λ_d is a dissipation scale, and λ_T is the Taylor microscale (Batchelor 1970; Pope 2000). For a weakly collisional plasma, such as the solar wind, the dissipation scale can be presumed to be the ion inertial length d_p or the ion thermal gyroradius (Verma 1996; Parashar et al. 2019; Cuesta et al. 2022), given that the inertial-range spectrum terminates (and then steepens) near these scales (Leamon et al. 1998; Smith et al. 2006; Matthaeus et al. 2008; Chen et al. 2014). Another scale related to dissipation is the Taylor microscale λ_T. This has been measured in the solar wind and then used to estimate effective Reynolds number for that system (Matthaeus et al. 2005, 2008; Chuychai et al. 2014; Bandyopadhyay et al. 2020b; Phillips et al. 2022). Note that both of the empirical determinations of effective Reynolds number given by Eq. (1) depend on the appropriate estimates of inner scales. Herein we adopt a

different approach that avoids any need to estimate inner scales. In a novel examination of the putative connection between collisional and collisionless dissipation, we explore specific evaluations of effective viscosity, resistivity, and Reynolds number from 2.5D and 3D kinetic Particle-in-Cell (PIC) simulations and *in situ* observations from the *Magnetosphere Multiscale* (MMS) mission.

2 THEORETICAL BACKGROUND

We are concerned with observed phenomena related to energy conversion processes and focus on the bulk flow energy, electromagnetic energy, thermal energy, and the conversion and dissipation channels that link them. For consistency in the contexts of observational and simulation data all quantities will be expressed in SI units throughout the paper.

2.1 Collisional cases

We start with the simplest one-fluid magnetohydrodynamic (MHD) model. The momentum and magnetic induction equations read,

$$\rho\frac{\partial \boldsymbol{u}}{\partial t} + \rho\boldsymbol{u} \cdot \nabla\boldsymbol{u} = -\nabla p - \nabla \cdot \boldsymbol{\Pi} + \boldsymbol{J} \times \boldsymbol{B}, \qquad (2)$$

$$\frac{\partial \boldsymbol{B}}{\partial t} - \nabla \times (\boldsymbol{u} \times \boldsymbol{B}) = \eta\nabla^2\boldsymbol{B}, \qquad (3)$$

where $\Pi_{ij} = -\mu\left(\partial_i u_j + \partial_j u_i\right) + \frac{2}{3}\mu(\nabla \cdot \boldsymbol{u})\delta_{ij}$ is the viscous stress tensor, $\boldsymbol{J} = \frac{1}{\mu_0}\nabla \times \boldsymbol{B}$ is the electric current, μ is the dynamic viscosity, η is the magnetic diffusivity, and $\mu_0 = 4\pi \times 10^{-7}$ [H $\cdot$ m^{-1}] is the magnetic permeability of free space (aka vacuum permeability).

Based on Eqs. (2) and (3) one readily obtains the collisional dissipation rates of bulk flow energy density ($E_u = \frac{1}{2}\rho\boldsymbol{u}^2$) and magnetic energy density ($E_b = \frac{1}{2\mu_0}\boldsymbol{B}^2$). These can be expressed in terms of the coefficients of dynamic viscosity (μ) and electrical resistivity ($1/\sigma \equiv \mu_0\eta$), and particular pieces of the velocity gradient and magnetic gradient tensors:

$$D_\mu = 2\mu D^2, \qquad (4)$$

$$D_\eta = \frac{1}{\sigma}J^2. \qquad (5)$$

Here $D_{ij} = \frac{1}{2}(\partial_i u_j + \partial_j u_i) - \frac{1}{3}(\nabla \cdot \boldsymbol{u})\delta_{ij}$ is the traceless strain rate tensor, with $D^2 = D_{ij}D_{ij}$ the second invariant of D_{ij} and equal to the sum of the squares of the eigenvalues of D_{ij}.

The viscous dissipation in Eq. (4) and the resistive dissipation in Eq. (5) are actually the *closures* of the anisotropic part of $-(\boldsymbol{P} \cdot \nabla) \cdot \boldsymbol{u}$ and the electric work $\boldsymbol{J} \cdot \boldsymbol{E}$ (see Eqs. (6)–(8)) in the presence of frequent collisions. These can be derived by kinetic methods (Chapman & Cowling 1939; Marshall 1960; Braginskii 1965; Kaufman 1960), where an approximate solution for the Boltzmann equation is firstly obtained in terms of macroscopic variables (like density, velocity, and temperature) and the pressure tensor (the second-order moment of the velocity distribution function) is then also expressed in terms of macroscopic variables. The closure of the electric work (i.e., Eq. (5)) can be derived using Ohm's law. The detailed procedure is: (i) In the presence of frequent collisions, it can be shown that no matter what the initial conditions are the velocity distribution function (VDF) f must approach a Maxwellian f_0 in a time of the order of the mean time between collisions (Chapman & Cowling 1939). (ii) The VDF f is assumed to be approximately a Maxwellian f_0 and high-order terms ($f_1, f_2, \cdots$) are introduced as small corrections or perturbations on the Maxwellian distribution function, $f = f_0 + f_1 + f_2 + \cdots$.

(iii) Retaining only the first-order correction f_1 and disregarding higher-order terms can give rise to the collisional dissipation, i.e., Eqs. (4) and (5).

To prescribe the applicability of the collisional approximation, we should keep in mind its requirement: *Even though the collisional dissipation provides a simple representation of dissipation in terms of the viscosity and resistivity, in all standard cases it applies only when the local distribution is very close to a Maxwellian due to particle collisions.*

2.2 Collisionless cases

The time evolution of energies can be derived using the first three moments of the Boltzmann equation, in conjunction with the Maxwell equations. One obtains (Braginskii 1965; Chiuderi & Velli 2015; Yang et al. 2017a,b)

$$\partial_t \mathcal{E}_\alpha^f + \nabla \cdot \left(\mathcal{E}_\alpha^f \boldsymbol{u}_\alpha + \boldsymbol{P}_\alpha \cdot \boldsymbol{u}_\alpha \right) = (\boldsymbol{P}_\alpha \cdot \nabla) \cdot \boldsymbol{u}_\alpha + \boldsymbol{J}_\alpha \cdot \boldsymbol{E}, \quad (6)$$

$$\partial_t \mathcal{E}_\alpha^{th} + \nabla \cdot \left(\mathcal{E}_\alpha^{th} \boldsymbol{u}_\alpha + \boldsymbol{h}_\alpha \right) = - (\boldsymbol{P}_\alpha \cdot \nabla) \cdot \boldsymbol{u}_\alpha, \quad (7)$$

$$\partial_t \mathcal{E}^m + \nabla \cdot \left(\boldsymbol{E} \times \frac{\boldsymbol{B}}{\mu_0} \right) = - \boldsymbol{J} \cdot \boldsymbol{E}, \quad (8)$$

where the subscript $\alpha = e, p$ represents the particle species (electrons and protons). Here, $\mathcal{E}^m = \frac{1}{2} \left(\epsilon_0 \boldsymbol{E}^2 + \boldsymbol{B}^2 / \mu_0 \right)$ is the electromagnetic energy density, with $\boldsymbol{E}, \boldsymbol{B}$ the electric and magnetic fields; $\mathcal{E}_\alpha^f = \frac{1}{2} \rho_\alpha \boldsymbol{u}_\alpha^2$ is the bulk flow energy density for species α, with mass density ρ_α and bulk flow velocity $\boldsymbol{u}_\alpha$; $\mathcal{E}_\alpha^{th} = \frac{1}{2} m_\alpha \int_v (\boldsymbol{v} - \boldsymbol{u}_\alpha) \cdot (\boldsymbol{v} - \boldsymbol{u}_\alpha) f_\alpha \, \mathrm{d}^3 v$ is the thermal energy, with mass m_α and velocity distribution function $f_\alpha(\boldsymbol{x}, \boldsymbol{v})$; $\boldsymbol{P}_\alpha$ is the pressure tensor; $\boldsymbol{h}_\alpha$ is the heat flux vector; $\boldsymbol{J} = \sum_\alpha \boldsymbol{J}_\alpha$ is the total electric current density with $\boldsymbol{J}_\alpha = n_\alpha q_\alpha \boldsymbol{u}_\alpha$ the electric current density of species α; $n_\alpha(\boldsymbol{x})$ and q_α are the number density and the charge of species α, respectively. As we can see the energy conversion between bulk flow and thermal is quantified by the pressure-strain interaction, $-(\boldsymbol{P}_\alpha \cdot \nabla) \cdot \boldsymbol{u}_\alpha$, while the energy conversion between bulk flow and electromagnetic is quantified by the electric work, $\boldsymbol{J} \cdot \boldsymbol{E}$. We emphasize that there are no $\boldsymbol{J}_\alpha$ terms in the thermal energy equation (7).

The basic assumption of collisional dissipation is that inter-particle collisions are sufficiently strong to maintain a local equilibrium. In principle, this assumption is not valid in collisionless plasmas. Instead, the particle VDF often displays a distorted out-of-equilibrium shape characterized by non-Maxwellian features as observed in *in situ* data (Graham et al. 2017; Perri et al. 2020) and in numerical simulations (Servidio et al. 2012). Although collisionless plasma can be described by the (collisional) MHD model at large scales, spacecraft *in situ* measurements reveal complex features at kinetic scales. At these small scales, kinetic processes must take place. One widely accepted picture of solar wind fluctuations is that they are characterised by broadband energy spectra with several spectral breaks and spectral steepening at kinetic scales (Leamon et al. 1998; Sahraoui et al. 2009; Alexandrova et al. 2009; Kiyani et al. 2015). In particular, observations indicate that the steepening of velocity and magnetic field spectra at kinetic scales is clearly dependent on the dissipation rate (Smith et al. 2006). Clearly collisionless dissipation delves deeply into kinetic plasma processes. Unlike collisional dissipation terminating at dissipation scales, collisionless dissipation is dominant at a range of kinetic scales.

2.3 Similarities between collisional and collisionless dissipation

Even though collisionless dissipation differs from collisional dissipation in several ways, studies also suggest that there are similarities between them. First, they are both organized in structured patterns and concentrated at, or near, coherent structures. Coherent structures form dynamically in MHD and plasma flows and are found to be of importance in heating. They include current sheets and vortices. According to the definition of collisional dissipation in Eqs. (4) and (5), it should not be at all surprising to find that the collisional dissipation occurs with intense values at (and near) these structures. The physical quantities that are responsible for the conversion of energy in collisionless plasmas (see Eqs. (6)-(8)) are also found in the same kind of spatial localization (Osman et al. 2011; Retinò et al. 2007; Yang et al. 2017a; Servidio et al. 2012; Franci et al. 2016; Parashar & Matthaeus 2016). In this sense, both collisional and collisionless dissipation concentrates in structured patterns. Second, they are both in direct association with velocity strain rate and electric current density. As we have already remarked, collisionless dissipation, as quantified by the electric work $\boldsymbol{J}_\alpha \cdot \boldsymbol{E}$ and the pressure-strain interaction $-(\boldsymbol{P}_\alpha \cdot \nabla) \cdot \boldsymbol{u}_\alpha$, is found to be in direct association with J^2 and D^2 (Chasapis et al. 2018; Bandyopadhyay et al. 2020a; Wan et al. 2016; Yang et al. 2017a; Bandyopadhyay et al. 2023), and this scaling is analogous to the resistive and viscous dissipation that Eqs. (4) and (5) represent.

We therefore conjecture that a closure for collisionless dissipation that is similar to collisional dissipation is plausible, in a statistical sense, the details of which are to be determined. That is, we suggest that

$$\langle -\Pi_{ij} D_{ij} | D \rangle \quad \sim \quad 2\mu D^2, \quad (9)$$

$$\langle \boldsymbol{J} \cdot \boldsymbol{E}' | J \rangle \quad \sim \quad \frac{1}{\sigma} J^2, \quad (10)$$

where $\Pi_{ij} = P_{ij} - p\delta_{ij}$ is the deviatoric pressure tensor, and $\boldsymbol{E}' = \boldsymbol{E} + \boldsymbol{u}_e \times \boldsymbol{B}$ is the electric field in the electron fluid frame. $\langle -\Pi_{ij} D_{ij} | D \rangle$ is the average of the anisotropic part of the pressure-strain interaction conditioned on $D \equiv \sqrt{D_{ij} D_{ji}}$, and $\langle \boldsymbol{J} \cdot \boldsymbol{E}' | J \rangle$ is the average of the electric work in the electron fluid frame conditioned on the (local) current magnitude $J = |\boldsymbol{J}|$. If the scalings in Eqs. (9) and (10) can be verified, they will permit an evaluation of effective values for dynamic viscosity μ and electrical resistivity $1/\sigma$, and thence for effective kinematic viscosity $\nu = \mu/\rho$ and magnetic diffusivity $\eta = 1/(\sigma \mu_0)$.

3 DATA

We present data from 2.5D and 3D fully kinetic PIC simulations and one long MMS burst-mode interval in the magnetosheath. In each case the analysis leads to a determination of the associated (effective) resistivity and separate viscosities for electrons and protons.

The *2.5D PIC simulation* employs the P3D code (Zeiler et al. 2002), which has also been used in Yang et al. (2022, 2023) and Bandyopadhyay et al. (2023). Here 2.5D means, as usual, that there are three components of dependent field vectors and a 2D spatial grid, i.e., that the phase space coordinates are (x, y, v_x, v_y, v_z). Normalization in P3D is largely "proton-based", with number density normalized to a reference value n_r, mass to proton mass m_p, charge to proton charge e, and magnetic field to a reference B_r. Length is normalized to the proton inertial length d_p, time to the proton cyclotron time ω_{cp}^{-1}, and velocity to the consequent reference Alfvén speed $V_{Ar} = B_r / (\mu_0 m_p n_r)^{1/2}$.

Dimension	L	N	m_p/m_e	$B_0\hat{z}$	$\delta b/B_0$	β	ppg
2.5D	$150\,d_p$	4096	25	1.0	0.5	0.6	3200
3D	$296\,d_e$	2048	50	0.5	1.0	0.5	150

Table 1. 2.5D and 3D PIC simulation parameters in code units: domain size L; grid points in each direction N; proton-to-electron mass ratio m_p/m_e; guide magnetic field in z-direction B_0; initial magnetic fluctuation amplitude δb; plasma β; average number of particles of each species per grid ppg.

The particular simulation we consider is performed in a square periodic domain of size $L = 150\,d_p$, with 4096^2 grid points and 3200 particles of each species per cell ($\sim 1.07 \times 10^{11}$ total particles). For numerical expediency we employ artificially low values of the proton to electron mass ratio, $m_p/m_e = 25$, and the speed of light, $c = 15\,V_{Ar}$. The run is a decaying initial value problem, starting with uniform densities and temperatures for both species. A uniform magnetic field, $B_0 = 1.0$, is directed out of the plane, and the initial plasma β is 0.6. The initial v and b fluctuations are transverse to B_0 ("Alfvén mode") and have Fourier modes with random phases for the wavenumber range $2 \le |kL/(2\pi)| \le 4$. The initial normalized cross helicity σ_c is negligible.

The *3D simulation* (Roytershteyn et al. 2015) is obtained using the VPIC code (Bowers et al. 2008), which was also used in Yang et al. (2022) and Bandyopadhyay et al. (2023). VPIC normalization differs significantly from that in P3D, being more electron based. Number density is normalized to a reference value n_r, mass to electron mass m_e, charge to proton charge e, length to the electron inertial length d_e, time to the electron plasma oscillation time ω_{pe}^{-1}, velocity to the (true physical) speed of light c, and magnetic field to a reference $B_r = m_e c \omega_{pe}/e$.

The simulation of interest herein was performed in a cubic periodic domain of size $L = 296\,d_e$, with 2048^3 grid points and 150 particles of each species per cell ($\sim 2.6 \times 10^{12}$ total particles). The proton to electron mass ratio is $m_p/m_e = 50$. Like the P3D run, this one is also a decaying initial value problem, starting with uniform density and temperature of protons and electrons. There is a uniform magnetic field $B_0 = 0.5$ in the out-of-plane $\hat{z}$ direction, and the plasma β is 0.5. The v and b fluctuations are initialized with two orthogonal polarizations and an overall power spectrum decaying as k^{-1} for the wavenumber range $1 \le |kL/(2\pi)| \le 7$ with equal power in each polarization. The initial v and b fluctuations are a mixture of Alfvénic and randomly phased perturbations. The initial normalized cross helicity is $\sigma_c \simeq 0.44$.

Key parameters for the 2.5D and 3D runs are given in Table 1. For both runs we analyze statistics at a time shortly after that at which the maximum mean square current density occurs. Prior to analyses, we remove noise inherent in the PIC plasma algorithm via a low-pass Fourier filtering of the fields.

In addition to simulation data we also analyze an interval of MMS spacecraft data. The MMS mission provides high time cadence and simultaneous multi-spacecraft measurements, typically in a tetrahedral formation, with small inter-spacecraft separations. The MMS spacecraft sample the near-Earth plasma including the magnetosheath (Burch et al. 2016). The proton and electron three-dimensional velocity distribution functions (VDFs) are available from the Fast Plasma Investigation (FPI) (Pollock et al. 2016) instrument. One can then determine density, velocity, pressure tensor, and current density, with a time resolution of 150 ms for ions and 30 ms for electrons. The Flux-Gate Magnetometer (FGM) (Russell et al. 2016) measures the vector

magnetic field, and the Electric Field Double Probes (EDP) (Ergun et al. 2016) measures the electric field. Herein we employ a single long-burst interval of MMS data obtained in the magnetosheath (see Table 3). For this interval the mean plasma velocity is approximately $230\,\mathrm{km\,s^{-1}}$ and the inter-spacecraft separation is about 27 km, which is below the ion inertial length and corresponds to a few times the electron inertial length. As shown in previous studies (Parashar et al. 2018; Bandyopadhyay et al. 2020a; Yang et al. 2023; Bandyopadhyay et al. 2023), this interval exhibits features of well-developed turbulence.

4 RESULTS

4.1 Kinematic Viscosity and Magnetic Diffusivity

To determine the values of the effective diffusion coefficients, we employ a method based on the recent work of Bandyopadhyay et al. (2023). The basic procedure, for the case of resistivity determination, is to compute $\langle J \cdot E'|J \rangle$, which is the average of the electric work in the electron fluid frame conditioned on the (local) current magnitude $J = |J|$, and investigate its dependence on J. As was noted previously (Wan et al. 2016; Bandyopadhyay et al. 2023), this conditional average is found to follow a curve $\langle J \cdot E'|J \rangle \sim J^2$ to a reasonable degree of accuracy, as shown here in the top row of Fig. 1. The error bars are computed from the standard deviation in each bin. Using this quadratic scaling agreement we evaluate the constants of proportionality for the two simulations and for the MMS data, thus providing an estimation of the effective resistivity for the respective cases. The functional form of the trend is strongly similar to that of the collisional case, as given in Eq. (5). This accounts for the heuristic description of the result as "collisional-like". These values of "effective resistivity" $1/\sigma$, within 95% confidence interval, are shown in the legend of Fig. 1 and tabulated in Table 3 in the respective units.

A similar procedure is followed for the the conditional average of the anisotropic part of the pressure-strain interaction, Pi-D$^{(\alpha)}$ ($= -\Pi_{ij}^{(\alpha)} D_{ij}^{(\alpha)}$), which represents the incompressible contribution to the rate of production of thermal energy (Braginskii 1965; Chiuderi & Velli 2015; Yang et al. 2022). This is done separately for electrons and protons. Specifically, we compute the average of electron Pi-D^e conditioned on $D^e \equiv \sqrt{D_{ij}^e D_{ji}^e}$, that is $\langle -\Pi_{ij}^e D_{ij}^e|D^e \rangle$. Recall that the traceless strain rate tensor for the electron fluid velocity is $D_{ij}^e = \frac{1}{2}(\partial_i u_j^e + \partial_j u_i^e) - \frac{1}{3}\delta_{ij}\nabla \cdot u^e$. The general trend is quite consistent with the collisional scaling in Eq. (4), as shown in the second row of Fig. 1. Thus the resulting approximation, that $\langle -\Pi_{ij}^e D_{ij}^e|D^e \rangle \propto (D^e)^2$, is indeed a collisional-like representation of the average results.

The analysis for the proton case proceeds in direct analogy to the electron case, with the results shown in the third row of Fig. 1. The conditional average of proton Pi-D^p is also found to be well approximated by a fit to a collisional-like scaling, as described in Eq. (4). That is, $\langle -\Pi_{ij}^p D_{ij}^p|D^p \rangle \propto (D^p)^2$, where D_{ij}^p is the traceless strain rate tensor for the proton fluid velocity and $D^p \equiv \sqrt{D_{ij}^p D_{ji}^p}$.

One might notice that, unlike the positive definite collisional dissipation in Eqs. (4) and (5), $\langle -\Pi_{ij}^{(\alpha)} D_{ij}^{(\alpha)}|D^{(\alpha)} \rangle$ is sign-indefinite, especially for the MMS data. Here we presume the existence of uniform viscosity and resistivity, without taking into account the sign effect. That is, for any negative conditional averages, we are taking their absolute values to fit the collisional scalings. A more careful and refined treatment of the sign effect is deferred to a future study.

All of the above results, including computations of the effec-

	$|\langle \boldsymbol{B} \rangle|$[nT]	$\delta B/|\langle \boldsymbol{B} \rangle|$	$\langle n_e \rangle$[cm^{-3}]	$\langle n_p \rangle$[cm^{-3}]	β_P	d_p[km]	d_e[km]	L[km]
2017 Dec 26 06:12:43-06:52:23	22.0	0.8	24.9	22.8	4.5	48	1.1	27

Table 2. Description of one selected magnetosheath interval of MMS data. $|\langle \boldsymbol{B} \rangle|$ is the mean magnetic field strength; $\delta B = \sqrt{\langle |\boldsymbol{B}(t) - \langle \boldsymbol{B} \rangle|^2 \rangle}$ is the root-mean-square magnetic fluctuation; $\langle n \rangle$ is the mean plasma density; β_P is the proton plasma beta; d_p and d_e the ion and electron inertial lengths; L indicates the mean separation between spacecraft.

tive kinematic viscosity ($\nu = \mu/\rho$) and magnetic diffusivity ($\eta = 1/(\sigma\mu_0)$) are shown in Table 3. Note that the diffusion coefficients from P3D and VPIC are expressed in the respective code units. To facilitate a direct comparison of the simulation numbers with MMS, we use the plasma properties measured for the MMS interval to convert the diffusion coefficients from code units to SI. That is, to compute the units in P3D, we need to use the proton inertial length d_p, proton cyclotron frequency ω_{cp}, Alfvén speed V_A, mean electron number density $\langle n_e \rangle$ measured over the MMS interval, and the real-life values of proton mass $m_p = 1.67 \times 10^{-27}$ kg and proton charge $e = 1.6 \times 10^{-19}$ C. Similarly, to compute the VPIC units, we need to use the electron inertial length d_e, electron plasma frequency ω_{pe}, mean electron number density $\langle n_e \rangle$ from the MMS interval, and the real-life values of electron mass m_e, proton charge e, and speed of light c. Finally, the effective kinematic viscosity and effective magnetic diffusivity from the two PIC simulations and the MMS interval are all expressed in SI units, m^2/s; see Table 4. Note that the viscosity and diffusivity are widely distributed for different datasets, reflecting the physical difference between the simulations and MMS data.

4.2 Empirical determination of Reynolds numbers

Given a diffusivity, a general prescription to obtain a Reynolds number (Re) is to assemble

$$\text{Re} = \frac{\text{speed} \times \text{length}}{\text{diffusivity}}, \quad (11)$$

where the speed and length are those characteristics of the turbulence. The results in the previous section make it possible to compute *effective Reynolds numbers* Re as described in Eq. (11), since we now have quantitative values for the (effective) diffusivities η, ν_e and ν_p. Choosing the correlation scales for the species velocities, $\lambda_{c,\alpha}$ ($\alpha = e, p$ for electrons and protons, respectively), and magnetic field, $\lambda_{c,b}$, as the characteristic lengths, we may write separate effective Reynolds numbers for the electron and protons, Re$_{c,\alpha}$, and an effective magnetic Reynolds number, Re$_{c,b}$, as

$$\text{Re}_{c,\alpha} = \frac{u_\alpha \lambda_{c,\alpha}}{\nu_\alpha}, \quad (12)$$

$$\text{Re}_{c,b} = \frac{u \lambda_{c,b}}{\eta}. \quad (13)$$

Here, u_α are the characteristic fluctuation speeds for each species. For the magnetic Reynolds number, the characteristic speed is denoted u and there is some flexibility in deciding what value to use for it.

The required values of *correlation scale* can be obtained as follows: The scale-dependent auto-correlation function is defined as

$$R(\boldsymbol{r}) = \frac{\langle \boldsymbol{F}(\boldsymbol{x} + \boldsymbol{r}) \cdot \boldsymbol{F}(\boldsymbol{x}) \rangle}{\langle \boldsymbol{F}(\boldsymbol{x}) \cdot \boldsymbol{F}(\boldsymbol{x}) \rangle}, \quad (14)$$

where $\boldsymbol{F}$ can be either the fluctuation velocity or magnetic field. Note that $R(\boldsymbol{r})$ is a function of lag vector $\boldsymbol{r} = (r_x, r_y, r_z)$. Upon

averaging over directions, $R(\boldsymbol{r})$ only depends on lag length $r = |\boldsymbol{r}|$, and $R(r)$ denotes the omnidirectional form of the auto-correlation function. Based on computation of the auto-correlation function, the correlation scale λ_c can be defined in several ways. Here we employ the so-called "e-folding" method,

$$R(\lambda_c) = 1/\text{e}, \quad (15)$$

where the correlation scale is computed as the scale where the auto-correlation function drops to $1/\text{e}$, on the basis that e^{-r/λ_c} is an adequate approximation for $R(r)$ (Matthaeus et al. 1999; Smith et al. 2018).

Figure 2 shows the results of our correlation analysis of simulation data and MMS observations. These results are employed to extract correlation lengths. The average bulk speed in this MMS interval is approximately $V_{SW} = 230 \text{ km s}^{-1}$, which is used to convert temporal scales to spatial scales for the MMS data. Characteristic fluctuation speeds and correlation scales for these three datasets are recorded in Table 5. As the two codes use different normalizations, Table 5 also indicates the relevant normalizing quantities, or units, in square brackets. Together with the (effective) kinematic viscosities and magnetic diffusivities listed in Table 3, these are combined in accordance with Eqs. (12) and (13) to compute the three corresponding effective Reynolds numbers, shown also in Table 5. Notably, for the simulation cases the three Reynolds numbers are all rather similar, whereas for the MMS interval there are sizable differences, which could be attributed to the uncertainties when computing the correlation length.

5 DISCUSSION AND CONCLUSIONS

This paper elaborates and extends the previous work by Bandyopadhyay et al. (2023) in which the initial analysis of conditional averages was presented, indicating that a collision-like dissipation may be present in collisionless plasma, as suggested by consistency of the data with Eqs. (9) and (10). Here we have quantitatively examined these approximate relations and determined effective viscosities for electrons and protons as well as an effective resistivity. This was carried out separately for two plasma kinetic (PIC) simulations, one 2.5D and one 3D, and for a sample of magnetosheath turbulence data recorded by the MMS mission. Having determined effective diffusion coefficients, and using measured fluctuation speeds and correlation scales, the assembly of effective Reynolds numbers follows directly.

From the effective large-scale Reynolds number, Re$_c$, relationships involving the plasma equivalent of the Kolmogorov *dissipation scale*, λ_D, may also be formulated,

$$\frac{\lambda_c}{\lambda_D} = C_\epsilon^{1/4} \text{Re}_c^{3/4}, \quad (16)$$

where C_ϵ is the dimensionless dissipation rate. This relation is formulated based on the classic development in hydrodynamic turbulence theory (Kolmogorov 1941a,b; Batchelor 1970), and may be used in several ways. One might substitute measured correlation scales λ_c
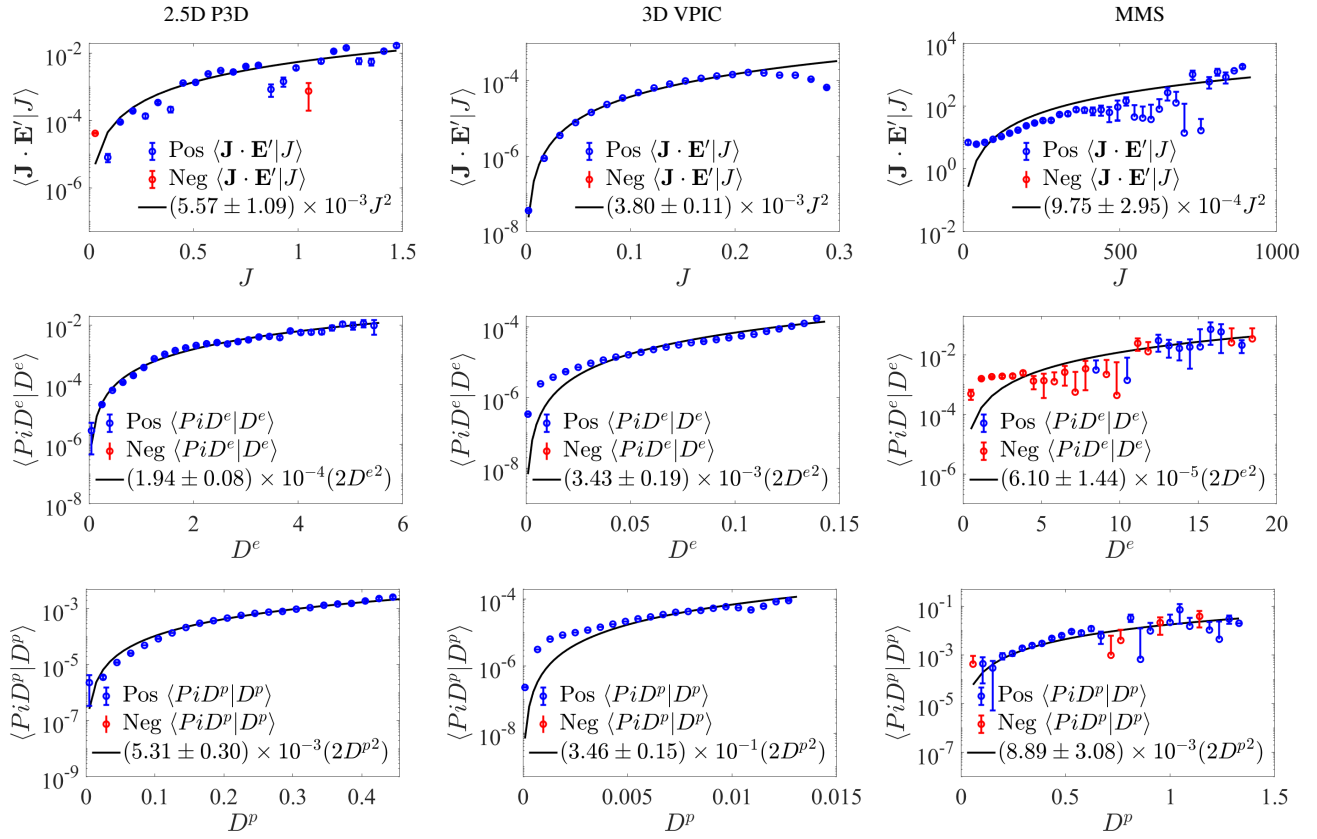
Figure 1. Conditional average of (top) the electromagnetic work $\mathbf{J} \cdot \mathbf{E}'$ with respect to the current density magnitude J, and (middle and bottom) Pi-D$^{(\alpha)}$ (= $-\Pi_{ij}^{(\alpha)} D_{ij}^{(\alpha)}$) with respect to the traceless velocity strain rate $D^{(\alpha)} = \sqrt{D_{ij}^{(\alpha)} D_{ij}^{(\alpha)}}$. The error bars are computed from the standard deviation in each bin. The coefficients from least-square fitting, within 95% confidence interval, are also shown.

Variables	2.5D P3D	3D VPIC	MMS
$\frac{1}{\sigma}$	$(5.57 \pm 1.09) \times 10^{-3}$ [$\frac{m_p \omega_{cp}}{n_r e^2}$]	$(3.80 \pm 0.11) \times 10^{-3}$ [$\frac{m_e \omega_{pe}}{n_r e^2}$]	$(9.75 \pm 2.95) \times 10^{-4}$ [$\frac{mV \cdot m}{nA}$]
$\eta = \frac{1}{\sigma \mu_0}$	$(4.43 \pm 0.87) \times 10^{3}$ [$\frac{m_p \omega_{cp}}{n_r e^2} \frac{m}{H}$]	$(3.02 \pm 0.09) \times 10^{3}$ [$\frac{m_e \omega_{pe}}{n_r e^2} \frac{m}{H}$]	$(7.76 \pm 2.35) \times 10^{8}$ [m^2/s]
μ_e	$(1.94 \pm 0.08) \times 10^{-4}$ [$m_p n_r V_{Ar} d_p$]	$(3.43 \pm 0.19) \times 10^{-3}$ [$m_e n_r c d_e$]	$(6.10 \pm 1.44) \times 10^{-5}$ [nPa · s]
$\nu_e = \frac{\mu_e}{\rho_e}$	$(4.85 \pm 0.20) \times 10^{-3}$ [$V_{Ar} d_p$]	$(3.43 \pm 0.19) \times 10^{-3}$ [$c d_e$]	$(2.69 \pm 0.64) \times 10^{9}$ [m^2/s]
μ_p	$(5.31 \pm 0.30) \times 10^{-3}$ [$m_p n_r V_{Ar} d_p$]	$(3.46 \pm 0.15) \times 10^{-1}$ [$m_e n_r c d_e$]	$(8.89 \pm 3.08) \times 10^{-3}$ [nPa · s]
$\nu_p = \frac{\mu_p}{\rho_P}$	$(5.31 \pm 0.30) \times 10^{-3}$ [$V_{Ar} d_p$]	$(6.92 \pm 0.30) \times 10^{-3}$ [$c d_e$]	$(2.33 \pm 0.81) \times 10^{8}$ [m^2/s]

Table 3. Effective electrical resistivity $1/\sigma$ and effective dynamic viscosity μ within 95% confidence interval from least-square fitting in Fig. 1, and the corresponding effective kinematic viscosity $\nu = \mu/\rho$ and effective magnetic diffusivity $\eta = 1/(\sigma \mu_0)$. The units are shown enclosed in square brackets and are those that apply to the specific code or data interval.

Variables	2.5D P3D	3D VPIC	MMS
η [m^2/s]	$(2.44 \pm 0.48) \times 10^{7}$	$(1.21 \pm 0.04) \times 10^{9}$	$(7.76 \pm 2.35) \times 10^{8}$
ν_e [m^2/s]	$(2.27 \pm 0.09) \times 10^{7}$	$(1.13 \pm 0.06) \times 10^{9}$	$(2.69 \pm 0.64) \times 10^{9}$
ν_P [m^2/s]	$(2.49 \pm 0.14) \times 10^{7}$	$(2.28 \pm 0.10) \times 10^{9}$	$(2.33 \pm 0.81) \times 10^{8}$

Table 4. Effective kinematic viscosity ν and effective magnetic diffusivity η from Table 3 re-expressed in SI units: m^2/s.
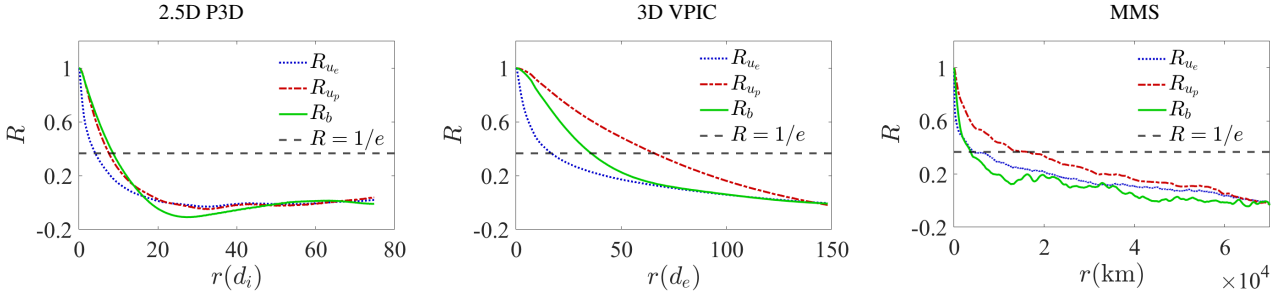
Figure 2. Correlation functions for the electron velocity, proton velocity, and magnetic field for the two PIC simulations and the MMS interval.

Variables	2.5D P3D	3D VPIC	MMS
$u_e = \sqrt{\langle \boldsymbol{u}_e^2 \rangle}$	0.30 [V_{Ar}]	0.055 [c]	232.8 [km/s]
$u_P = \sqrt{\langle \boldsymbol{u}_P^2 \rangle}$	0.22 [V_{Ar}]	0.032 [c]	242.1 [km/s]
$\lambda_{c,e}$	4.1 [d_p]	17 [d_e]	4380 [km]
$\lambda_{c,p}$	7.5 [d_p]	65 [d_e]	15990 [km]
$\lambda_{c,b}$	8.5 [d_p]	36 [d_e]	3690 [km]
$\mathrm{Re}_{c,e} = u_e \lambda_{c,e}/\nu_e$	250	270	380
$\mathrm{Re}_{c,p} = u_p \lambda_{c,p}/\nu_p$	320	300	16610
$\mathrm{Re}_{c,b} = u_p \lambda_{c,b}/\eta$	370	310	1150

Table 5. Characteristic fluctuation speeds u, correlation scales λ_c, and effective large-scale Reynolds numbers Re_c. Additional e, p, and b subscripts indicate the quantity for the electrons, protons, or magnetic field, respectively. Here the characteristic fluctuation speed for protons, u_P, is used to compute the effective magnetic Reynolds number.

and effective Reynolds numbers Re_c into the formula to extract an estimate of the dissipation scale λ_D. Alternatively one might assume, as has been done previously, that the dissipation scale in a plasma such as solar wind, corresponds to the upper end of the inertial range. Then if the value of λ_D is taken to be, for example the ion (or electron) inertial length d_p (or d_e), Eq. (16) may be construed as providing another alternative estimate of (effective) Reynolds number. There are also other approaches for estimating the dissipation scale. For example, if the cascade rate ϵ is known and an effective viscosity is available, hydrodynamic turbulence theory provides the Kolmogorov-style estimate $\lambda_D = \left(\nu^3/\epsilon\right)^{1/4}$.

The Reynolds numbers determined here are roughly consistent with reasonable estimates of the corresponding dissipation scales, through the formulation given by Eq. (16). For example, substituting the proton Reynolds number $\mathrm{Re}_{c,p} = 320$ for the 2.5D simulations into Eq. (16) and using a value $C_\epsilon = 0.5$ (as in, e.g., Linkmann et al. (2017); Bandyopadhyay et al. (2018); Li et al. (2023)) and the measured correlation scale $\lambda_{c,p} = 7.5\, d_p$, the relation Eq. (16) gives $\lambda_D \sim 0.1\, d_p$, which is not an unreasonable estimation. For the MMS data, the same line of analysis leads to the estimate $\lambda_D \sim 13$ km. This too is a reasonable estimate for the dissipation scale in the magnetosheath, where for this interval the value of d_p is 48 km (see Table 3). In fact, there are several other ways to combine the above values of Reynolds numbers and measured parameters to examine consistency with traditional estimates. All the combinations we have tried provide reasonable answers, such as values of λ_D

that are deemed reasonable given the findings from simulations and other observations that spectral steepening usually occurs near d_p. However, no firm guidance is available providing a more detailed picture of a scale at which electron and proton dissipation become dominant or "turn on" relative to each other. See, for example, Yang et al. (2022).

Another interesting aspect of the present results is the size of the (effective) magnetic Prandtl number *Pm*, generally defined as the ratio of kinematic viscosity ν to magnetic diffusivity η. Here, examining the values of the effective magnetic diffusivity and two viscosities stated in Table 4, we see that the magnetic Prandtl number estimates from both simulation results are near unity. For the MMS data, the value is only moderately away from unity. The significance of this is that when *Pm* greatly differs from unity, different regimes of MHD scale behavior become possible (Cho et al. 2002; Ponty et al. 2005; Sahoo et al. 2011). In particular, in such cases the inertial ranges in magnetic field and velocity field can develop very different bandwidths. A value of *Pm* near unity is consistent with the usual finding of "Alfvénic" turbulence in which there is order one equipartition of magnetic and velocity field energy in their respective inertial ranges over very similar ranges of wavenumber.

We remark that although the classical collisional diffusivity must obviously be absent in collisionless plasmas, a number of previous works have nonetheless attempted to write approximate expressions for effective diffusion coefficients in collisionless plasma. Possible candidates that act as effective collisions include wave-particle interactions (Graham et al. 2022), pitch angle scattering (Earl et al. 1988; Zank et al. 2014), stochastic field line effects, and other kinetic mechanisms. In particular viscosity and resistivity have been estimated based on various approximations; for the present, we leave aside the estimation of other transport coefficients such as heat conduction (Hollweg 1976; Riquelme et al. 2016). Resistivity is often estimated using terms in the generalized Ohm's law in terms of fluid quantities (Graham et al. 2022; Selvi et al. 2023), or in the case of hyper-resistivity, by consideration of contributions from anomalous electron viscosity (Strauss 1986). A collisional-like viscosity is already present in earlier studies, such as gyroviscosity (Smolyakov 1998), cosmic-ray viscosity (Earl et al. 1988), and plasma viscosity (Kaufman 1960). Viscous effects are often estimated by consideration of the MHD-scale cascade and its implications for pressure anisotropies (Quataert & Gruzinov 1999; Sharma et al. 2007; Verma 2019). Considerations of pressure anisotropy (Kasper et al. 2002; Matteini et al. 2007) and linear instabilities that drive it, can be employed to develop theories for effective viscosity. This may be particularly effective when combined with exact results from Vlasov–Maxwell theory, such as dissipation through the pressure-strain interaction (Yang et al. 2017a). Such considerations have motivated more elaborate approximate models for effective viscosity based on

pressure anisotropy in the simplified CGL model (Squire et al. 2023; Arzamasskiy et al. 2023). Valuable insights are obtained from models of this type, especially with regard to extrapolations to extreme values of plasma β that can be relevant to astrophysical systems (Kawazura et al. 2019; Howes 2010; Roy et al. 2022).

Finally, we recall that several additional relationships may be adapted from classical turbulence theory to provide alternative estimates for Reynolds numbers and diffusivities. One possibility is to base measurements on the Taylor microscale λ_T, which can be related directly to the second derivative of the auto-correlation function evaluated at the origin (e.g., Batchelor 1970; Pope 2000). Up to order unity constants, $\lambda_T = [-R''(0)]^{-1/2}$, where we have in mind that $R(r)$ is the direction averaged correlation function of, say, the magnetic field, as in Eq. (14). Then one can show that an estimate of the effective Reynolds number can be written as Re $= (\lambda_c/\lambda_T)^2/C_\epsilon$. This quantity is measurable when high-resolution data is available, and may be further developed into an estimate of the effective viscosity, as shown by Bandyopadhyay et al. (2020b). The above relationships should be viewed as semi-empirical and, while motivated by theory, should not be treated as exact in any sense, since the underlying theories are mainly hydrodynamic (and collisional) and usually founded on simple assumptions of rotational symmetry or incompressibility.

Based on the above results and given the unique nature of the analysis developed so far, we conclude that the present approach to quantifying collisional-like dissipation in collisionless plasma turbulence warrants further investigation. Already we have seen herein that examination of conditional averages of pressure-strain interaction and electric work, which themselves are exact statements of energy conversion rates, provides a basis for finding effective diffusion coefficients. With apparently reasonable values of (effective) Reynolds numbers, viscosities, and resistivities in hand, the door is opened to examining a class of relationships that may help bring turbulence theory concepts into greater contact with turbulent plasma, as we have described above. There is clearly much more to do in the complex subject of plasma turbulence, and the present work offers a small step in a possibly useful direction.

DATA AVAILABILITY

This study used Level 2 FPI and FIELDS data according to the guidelines set forth by the MMS instrumentation team. The data that support the findings of this study are openly available in MMS SDC at https://lasp.colorado.edu/MMS/sdc/. Other reasonable requests for sharing of the metadata regarding computational runs, custom simulation codes and documentation will generally be honored.

REFERENCES

Alexandrova O., Saur J., Lacombe C., Mangeney A., Mitchell J., Schwartz S. J., Robert P., 2009, Phys. Rev. Lett., 103, 165003

Andrés N., Sahraoui F., Galtier S., Hadid L. Z., Ferrand R., Huang S. Y., 2019, Physical review letters, 123, 245101

Arzamasskiy L., Kunz M. W., Squire J., Quataert E., Schekochihin A. A., 2023, Phys. Rev. X, 13

Bandyopadhyay R., Oughton S., Wan M., Matthaeus W. H., Chhiber R., Parashar T. N., 2018, Phys. Rev. X, 8, 041052

Bandyopadhyay R., et al., 2020a, Phys. Rev. Lett., 124, 255101

Bandyopadhyay R., et al., 2020b, Astrophys. J., 899, 63

Bandyopadhyay R., et al., 2023, Phys. Plasmas, 30, 080702

Banerjee S., Andrés N., 2020, Physical Review E, 101, 043212

Batchelor G. K., 1970, The Theory of Homogeneous Turbulence. Cambridge University Press, Cambridge, UK

Bowers K. J., Albright B. J., Yin L., Bergen B., Kwan T. J. T., 2008, Phys. Plasmas, 15

Braginskii S. I., 1965, Rev. Plasma Phys., 1, 205

Bruno R., Carbone V., 2013, Living Reviews in Solar Physics, 10, 2

Burch J. L., et al., 2016, Science

Chandran B. D. G., Li B., Rogers B. N., Quataert E., Germaschewski K., 2010, Astrophys. J., 720, 503

Chapman S., Cowling T. G., 1939, The mathematical theory of non-uniform gases: An account of the kinetic theory of viscosity, thermal conduction and diffusion in gases. Cambridge University Press

Chasapis A., et al., 2018, Astrophys. J. Lett., 856, L19

Chen C. H. K., Leung L., Boldyrev S., Maruca B. A., Bale S. D., 2014, Geophys. Res. Lett., 41, 8081

Chiuderi C., Velli M., 2015, Basics of Plasma Astrophysics. Springer

Cho J., Lazarian A., Vishniac E. T., 2002, Astrophys. J., 564, 291

Chuychai P., Weygand J. M., Matthaeus W. H., Dasso S., Smith C. W., Kivelson M. G., 2014, J. Geophys. Res., 119, 4256

Coleman P. J., 1968, Astrophys. J., 153, 371

Cuesta M. E., Parashar T. N., Chhiber R., Matthaeus W. H., 2022, Astrophys. J. Suppl. Ser, 259, 23

Dmitruk P., Matthaeus W. H., Seenu N., 2004, Astrophys. J., 617, 667

Earl J. A., Jokipii J. R., Morfill G., 1988, The Astrophysical Journal, 331, L91

Ergun R. E., et al., 2016, Space Sci. Rev., 199, 167

Franci L., Landi S., Matteini L., Verdini A., Hellinger P., 2016, Astrophys. J., 833, 91

Graham D. B., et al., 2017, Physical Review Letters, 119, 025101

Graham D., et al., 2022, Nature Communications, 13, 1

Hadid L. Z., Sahraoui F., Galtier S., 2017, Astrophys. J., 838, 9

Hellinger P., Montagud-Camps V., Franci L., Matteini L., Papini E., Verdini A., Landi S., 2022, The Astrophysical Journal, 930, 48

Hollweg J. V., 1976, J. Geophys. Res., 81, 1649

Hossain M., Gray P. C., Pontius Jr. D. H., Matthaeus W. H., Oughton S., 1995, Phys. Fluids, 7, 2886

Howes G. G., 2010, Mon. Not. R. Astron. Soc., 409, L104

Howes G. G., Dorland W., Cowley S. C., Hammett G. W., Quataert E., Schekochihin A. A., Tatsuno T., 2008, Phys. Rev. Lett., 100, 065004

Kasper J. C., Lazarus A. J., Gary S. P., 2002, Geophys. Res. Lett., 29, 20

Kaufman A. N., 1960, The Physics of Fluids, 3, 610

Kawazura Y., Barnes M., Schekochihin A. A., 2019, Proc. Nat. Acad. Sci. USA, 116, 771

Kiyani K. H., Osman K. T., Chapman S. C., 2015, Phil. Trans. R. Soc. A, 373, 20140155

Kolmogorov A. N., 1941a, Dokl. Akad. Nauk SSSR, 30, 301

Kolmogorov A. N., 1941b, C.R. Acad. Sci. U.R.S.S., 32, 16

Leamon R. J., Smith C. W., Ness N. F., Matthaeus W. H., Wong H. K., 1998, J. Geophys. Res., 103, 4775

Li C., Yang Y., Matthaeus W., Jiang B., Wan M., Chen S., 2023, submitted to Physical Review Letters

Linkmann M., Berera A., Goldstraw E. E., 2017, Phys. Rev. E, 95, 013102

Markovskii S. A., Vasquez B. J., Smith C. W., Hollweg J. V., 2006, Astrophys. J., 639, 1177

Marsch E., 2006, Living Rev. Solar Phys., 3

Marshall W., 1960, The kinetic theory of an ionized gas. Vol. 2247, Atomic Energy Research Establishment

Matteini L., Landi S., Hellinger P., Pantellini F., Maksimovic M., Velli M., Goldstein B. E., Marsch E., 2007, Geophys. Res. Lett., 34

Matthaeus W. H., Zank G. P., Smith C. W., Oughton S., 1999, Phys. Rev. Lett., 82, 3444

Matthaeus W. H., Dasso S., Weygand J. M., Milano L. J., Smith C. W., Kivelson M. G., 2005, Phys. Rev. Lett., 95, 231101

Matthaeus W. H., Weygand J. M., Chuychai P., Dasso S., Smith C. W., Kivelson M. G., 2008, Astrophys. J., 678, L141

Osman K. T., Matthaeus W. H., Greco A., Servidio S., 2011, Astrophys. J. Lett., 727, L11

Parashar T. N., Matthaeus W. H., 2016, Astrophys. J., 832, 57

Parashar T. N., Servidio S., Shay M. A., Breech B., Matthaeus W. H., 2011, Phys. Plasmas, 18

Parashar T. N., et al., 2018, Phys. Rev. Lett., 121, 265101

Parashar T. N., Cuesta M., Matthaeus W. H., 2019, Astrophys. J., 884, L57

Perri S., et al., 2020, Journal of Plasma Physics, 86

Phillips C., Bandyopadhyay R., McComas D. J., 2022, Astrophys. J., 933, 33

Politano H., Pouquet A., 1998, Geophys. Res. Lett., 25, 273

Pollock C., et al., 2016, Space Sci. Rev., 199, 331

Ponty Y., Mininni P. D., Montgomery D. C., Pinton J.-F., Politano H., Pouquet A., 2005, Phys. Rev. Lett., 94

Pope S. B., 2000, Turbulent Flows. Cambridge University Press, Cambridge, UK

Quataert E., Gruzinov A., 1999, Astrophys. J., 520, 248

Retinò A., Sundkvist D., Vaivads A., Mozer F., André M., Owen C. J., 2007, Nat. Phys., 3, 236

Riquelme M. A., Quataert E., Verscharen D., 2016, Astrophys. J., 824, 123

Roy S., et al., 2022, Astrophys. J., 941, 137

Roytershteyn V., Karimabadi H., Roberts A., 2015, Phil. Trans. R. Soc. A, 373, 20140151

Russell C. T., et al., 2016, Space Sci. Rev., 199, 189

Sahoo G., Perlekar P., Pandit R., 2011, New J. Phys., 13, 013036

Sahraoui F., Goldstein M. L., Robert P., Khotyaintsev Y. V., 2009, Phys. Rev. Lett., 102, 231102

Selvi S., Porth O., Ripperda B., Bacchini F., Sironi L., Keppens R., 2023, Astrophys. J., 950, 169

Servidio S., Valentini F., Califano F., Veltri P., 2012, Phys. Rev. Lett., 108

Sharma P., Quataert E., Hammett G., Stone J. M., 2007, Astrophys. J., 667, 714

Smith C. W., Hamilton K., Vasquez B. J., Leamon R. J., 2006, Astrophys. J., 645, L85

Smith C. W., Vasquez B. J., Coburn J. T., Forman M. A., Stawarz J. E., 2018, Astrophys. J., 858, 21

Smolyakov A. I., 1998, Canadian Journal of Physics, 76, 321

Sorriso-Valvo L., et al., 2007, Phys. Rev. Lett., 99

Squire J., Kunz M. W., Arzamasskiy L., Johnston Z., Quataert E., Schekochihin A. A., 2023, arXiv preprint arXiv:2303.00468

Strauss H., 1986, Phys. Fluids, 29, 3668

Verma M. K., 1996, J. Geophys. Res., 101, 27 543

Verma M. K., 2019, European Physical Journal B, 92, 190

Verniero J., et al., 2020, The Astrophysical Journal Supplement Series, 248, 5

Wan M., Oughton S., Servidio S., Matthaeus W. H., 2012, J. Fluid Mech., 697, 296

Wan M., Matthaeus W. H., Roytershteyn V., Parashar T. N., Wu P., Karimabadi H., 2016, Phys. Plasmas, 23

Yang Y., et al., 2017a, Phys. Plasmas, 24, 072306

Yang Y., et al., 2017b, Phys. Rev. E, 95, 061201

Yang Y., Matthaeus W. H., Roy S., Roytershteyn V., Parashar T. N., Bandyopadhyay R., Wan M., 2022, Astrophys. J., 929, 142

Yang Y., et al., 2023, Astrophys. J., 944, 148

Zank G., Hunana P., Mostafavi P., Goldstein M., 2014, The Astrophysical Journal, 797, 87

Zank G. P., Adhikari L., Hunana P., Shiota D., Bruno R., Telloni D., 2017, Astrophys. J., 835, 147

Zeiler A., Biskamp D., Drake J. F., Rogers B. N., Shay M. A., Scholer M., 2002, J. Geophys. Res., 107, 1230

Zenitani S., Hesse M., Klimas A., Kuznetsova M., 2011, Phys. Rev. Lett., 106, 195003

de Kármán T., Howarth L., 1938, Proc. Roy. Soc. London Ser. A, 164, 192

This paper has been typeset from a TeX/LaTeX file prepared by the author.